metals

MDPI

Article

Synthesis of Core-Shell Carbon Encapsulated Fe_2O_3 Composite through a Facile Hydrothermal Approach and Their Application as Anode Materials for Sodium-Ion Batteries

Yongguang Zhang [1], Zhumabay Bakenov [2], Taizhe Tan [1,*] and Jin Huang [1,*]

[1] School of Materials and Energy, Synergy Innovation Institute of GDUT, Guangdong University of Technology, Guangzhou 510006, China; ygzhang126@126.com

[2] Institute of Batteries LLC, School of Engineering, National Laboratory Astana, Nazarbayev University, 53 Kabanbay Batyr Avenue, Astana 010000, Kazakhstan; zbakeno@nu.edu.kz

* Correspondence: tztansii18@163.com (T.T.); huangjiner@126.com (J.H.)

Received: 24 May 2018; Accepted: 15 June 2018; Published: 18 June 2018

Abstract: Carbon encapsulated Fe_2O_3 nanoparticles ($C@Fe_2O_3$) were successfully synthesized via a facile and environmentally friendly hydrothermal method and prototyped in anode materials for sodium ion batteries (SIBs). High-resolution transmission and scanning electronic microscopy observations exhibited the formation of a highly core-shelled $C@Fe_2O_3$ composite consisting of carbon layers coated onto uniform Fe_2O_3 nanoparticles with a median diameter of 46.1 nm. This core-shell structure can repress the aggregation of Fe_2O_3 nanoparticles, preventing the harsh volume change of the electrode, enhancing the electric conductivity of the active materials, and promoting Na-ion transformation during cycling. The electrochemical performances of the $C@Fe_2O_3$ composite, as anodes for SIBs, retained a reversible capacity of 305 mAh g^{-1} after 100 cycles at 50 mA g^{-1} and exhibited an excellent cyclability at various current densities due to the synergistic effect between the carbon layers and Fe_2O_3. These results suggest that $C@Fe_2O_3$ composites present much potential as anode materials for rechargeable SIBs.

Keywords: $C@Fe_2O_3$ composite; anode; sodium ion battery

1. Introduction

Recently, sodium-ion batteries (SIBs) have attracted intensive attention as an alternative to lithium-ion batteries (LIBs). This interest can be attributed to the fact that sodium is abundantly available and is economically cheaper than lithium [1,2]. Graphite was established as the gold-standard anode material for lithium ion batteries (LIBs) due to their modest reversible capacity (372 mAh g^{-1}), superior cycling behavior, high Coulombic efficiency, low cost, and low and flat potential plateaus, which provide a decent voltage window [3]. However, conventional graphite is not suitable for SIB anodes because the larger atomic radius of sodium requires intercalation hosts, with larger diffusion channels [4]. In recent years, the researched anode materials for SIBs transition metal oxides, such as TiO_2, ZnO, and Co_3O_4, were found to hold the greatest potential for anode materials in SIBs due to their exceptional theoretical capacities, good versatility, and cost advantages [5–10]. In general, these anodes face severe challenges in poor electronic conductivity and huge volume changes during cycling. Therefore, the development of anode materials with excellent electrochemical performances is crucial. In particular, Fe_2O_3, which possess a lofty theoretical specific capacity (1007 mAh g^{-1}) [11], has garnered much attention in recent years [8–11]. However, the cycling stability of the Fe_2O_3 anode is significantly hindered by the harsh volume expansion/contraction during the Na alloying/dealloying

processes. To boost the stability of the Fe_2O_3 anode and better the capacity retention and cycle life, an effective strategy, which has been previously investigated, is to combine Fe_2O_3 nanoparticles with carbonaceous substances. For example, Wang's group reported the preparation of α-Fe_2O_3/RGO composites via microwave autoclave, with the resulting nanocomposites delivering a capacity of 310 mAh g^{-1} after 150 cycles at 100 mA g^{-1} [12].

In lithium-ion batteries, the carbon encapsulated Fe_2O_3 nanoparticles (C@Fe_2O_3) as anode materials attract special interest of researchers since this core-shell structured nanocomposite exhibits enhanced physical and chemical properties [13]. Coating layers of carbon onto a Fe_2O_3 core will simultaneously improve the electric conductivity and act as a buffer layer to mitigate the mechanical strain and improve the mechanical integrity due to the ductile and elastic nature of carbonaceous materials [14,15]. All these merits are beneficial for the development of electrochemical performance. Encouraged by these promising and interesting works, herein, we prepared core-shell structure C@Fe_2O_3 composites by a one-step hydrothermal procedure. Carbon layers were homogenously coated on the Fe_2O_3 nanoparticles, with a median diameter of 46.1 nm. From this unique design, the C@Fe_2O_3 composites exhibit an impressive Na-ion storage performance with a high capacity and good cycles.

2. Materials and Methods

2.1. Materials Preparation

The C@Fe_2O_3 composites with a core-shell structure were synthesized by the hydro-thermal method. Glucose (0.3 g) and iron nitrate hydrate (0.4 g) were dispersed in distilled water (40 mL) using a thermostatic magnetic mixer (Zhengzhou Teer Instruments, Zhengzhou, China) for 0.5 h to form a uniform suspension. Subsequently, the mixed solution was displaced to reaction still after 0.25 h sonication using an ultrasonic cell disruptor (Ningbo Scientz Biotechnology Co., Ningbo, China), then heated in a 40 mL Teflon-lined stainless-steel autoclave for 9 h at 190 °C, and then left in ambient conditions. After cooling to room temperature, the products were washed thoroughly via centrifugal with deionized water. Finally, the washed products were dried under vacuum at 80 °C for 24 h to prepare carbon encapsulated Fe_2O_3 nanoparticles in a core-shell structure.

2.2. Materials Characterization

The crystal phase of C@Fe_2O_3 composites was analyzed by Rigaku D/Max 2500V/pc X-ray diffractometer (XRD) (Rigaku-TTRIII, Tokyo, Japan) with Cu Kα (λ = 1.5406 Å) in scanning step of 0.02°. The morphology was observed by a JEOL JSM-6700F scanning electron microscope (SEM, equipped with EDX elemental analysis, JEOL, Tokyo, Japan) and high-resolution transmission electron microscopy (HR-TEM, JEOL, Tokyo, Japan) from a JEOL JEM-2100F instrument with 200 kV acceleration voltage. Brunauer Emmett Teller (BET) (V-Sorb 2800P) tests were conducted to investigate the specific surface area of the composites. X-ray photoelectron spectroscopy (XPS) data was obtained with a PHI 5000 Versa Probe system (Ulvac-Phi, Kanagawa, Japan). The carbon content was estimated by thermo gravimetric analysis (TGA, SDTQ600, TA Instruments-Waters LLC, Newcastle, PA, USA). Raman spectroscopy analysis was examined on Raman spectroscopy (LabRAM Hr 800, HORIBA Jobin Yvon, Paris, France) with the laser wavelength of 514 nm.

2.3. Electrochemical Measurements

The electrochemical measurements were conducted at room temperature using coin cells (CR2025), with a sodium foil as the counter and reference electrode. The working electrode consisted of a C@Fe_2O_3 slurry, acetylene black, and sodium alginate binder combined at a weight ratio, 7:2:1, and evenly applied onto copper foil with 15 mm in diameter. The as-prepared working electrodes were dried in a vacuum oven at 80 °C for over 12 h to remove any residual moisture. The electrolyte was comprised of 1 M $NaClO_4$ dissolved in a mixture of ethylene carbonate and dimethyl carbonate (1:1 by volume),

and the separator used was a glass fiber film. The electrochemical performances were probed between 0.01 and 3.0 V (vs. Na/Na^+) with a battery testing system (BTS-5V5 mA, Neware, Shenzhen, China). The specific capacity was calculated in reference to the mass of the total active material.

3. Results and Discussion

The crystalline structure of the $C@Fe_2O_3$ composite was characterized by XRD. Figure 1 shows that the typical diffraction peaks at 30.3°, 35.7°, 57.4°, and 63.1°, which correspond to the reflections of (2 0 6), (1 1 9), (1 1 15), and (4 0 12) planes of the Fe_2O_3 structure (JPDS No. 25-1402), respectively. There is no evident carbon peak due to the presence of amorphous carbon.

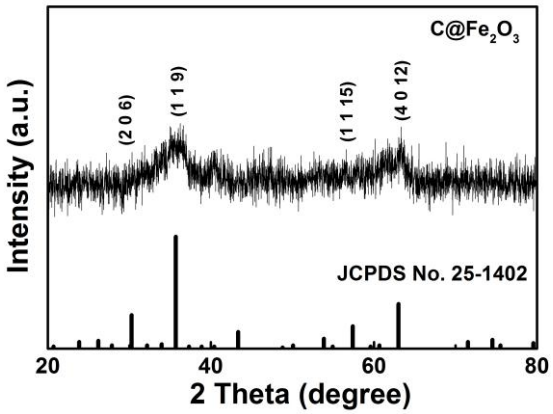

Figure 1. X-ray diffractometer (XRD) patterns of the $C@Fe_2O_3$ composite.

Raman spectra further confirmed the presence of carbon in the composites. As shown in Figure 2, two obvious bands at 1350 and 1586 cm^{-1} are assigned to typical D and G bands of carbon, respectively. A 2D band of 2693 cm^{-1} is also observed, confirming the presence of carbon from the hydro-thermal process of glucose in the composites.

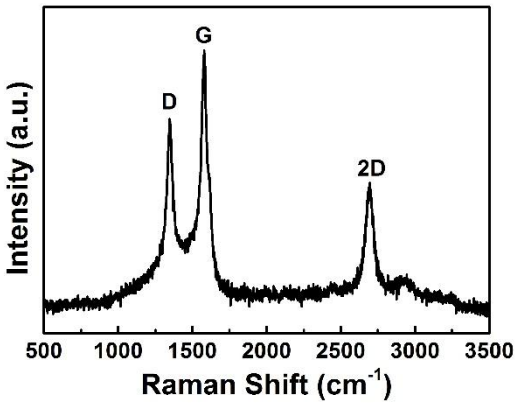

Figure 2. Raman spectrum of the $C@Fe_2O_3$ composite.

The morphology and particle sizes of $C@Fe_2O_3$ composites were characterized by SEM measurements. As shown in Figure 3a,b, the $C@Fe_2O_3$ composites are uniform spheres, with a median diameter of approximately 50 nm. The inset in Figure 3b depicts the average diameter of the $C@Fe_2O_3$ composites was 46.1 nm. The structure of the $C@Fe_2O_3$ composite was further investigated by TEM. Figure 3c illustrates carbon wrapping of Fe_2O_3 nanoparticles, which possess an average diameter of ~10 nm, confirming a core-shell structure. The HRTEM analysis, shown in Figure 3d, reveals the lattice fringe, with a distance spacing of 0.238 nm, corresponding to the (2 2 6) plane of Fe_2O_3. The image also

illustrates that the thickness of the carbon layer was approximately 0.83 nm. The energy dispersive spectrometer (EDS) element mapping, shown in Figure 4, clearly demonstrates that the C@Fe_2O_3 composite mainly consist of C, Fe, and O, with a uniform distribution.

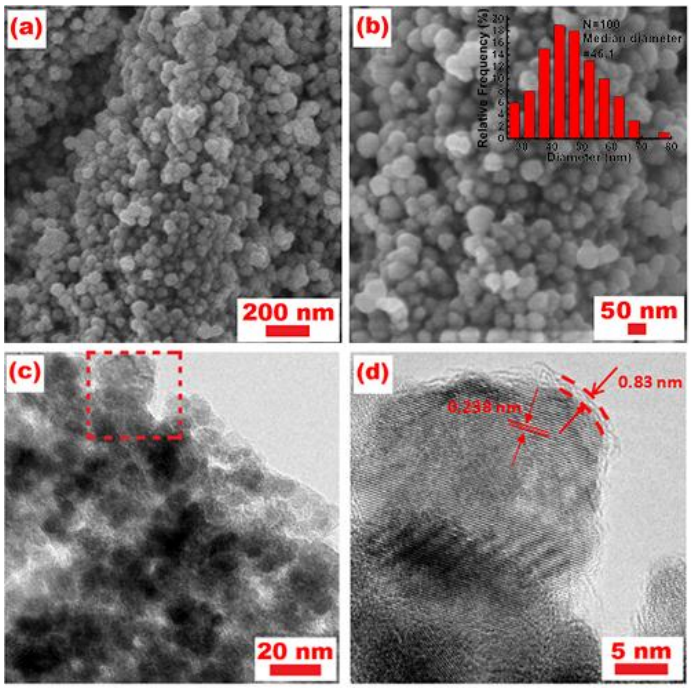

Figure 3. SEM images (**a**,**b**) and corresponding median diameter (inset) and TEM images (**c**,**d**) of the C@Fe_2O_3 composites.

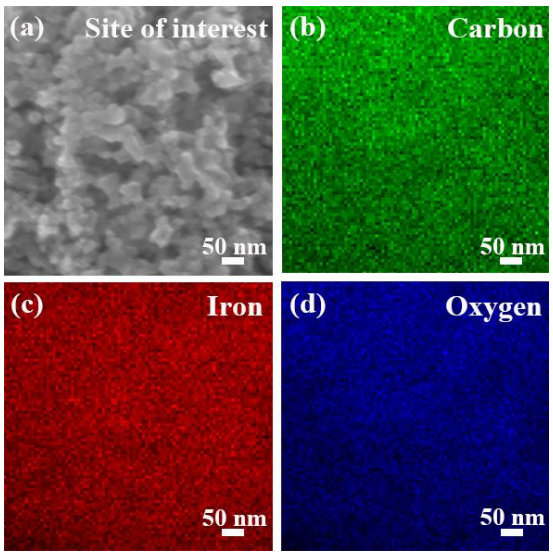

Figure 4. SEM image (**a**) of the C@Fe_2O_3 composite and corresponding carbon (**b**), iron (**c**), and oxygen (**d**) element mapping.

The chemical composition and chemical bonding were further investigated by XPS, shown in Figure 5. As shown in Figure 5a, the peaks of Fe 2p, C 1s, and O 1s were detected in the C@Fe_2O_3 composite. Figure 5b delivers two peaks located at 724.7 and 711.1 eV in the high-resolution Fe 2p spectra, corresponding to Fe 2p1/2 and Fe 2p3/2, respectively. In addition, two weak satellite peaks at 733.3 and 719.5 eV can be attributed to the Fe 2p1/2 and Fe 2p3/2, respectively. This phenomenon

indicates that the composite was composed of Fe^{3+} only. Figure 5c shows three peaks at 288.6, 286.6, and 284.8 eV in the C 1s spectra, corresponding to the C=O, C–O–C, and C–C, respectively. Figure 5d shows two peaks located at 531.8 and 529.8 eV in the O 1s spectra, which is attributed to Fe–O–H and Fe–O, respectively. Overall, the results indicate the successful transformation of glucose and iron nitrate hydrate into C@Fe_2O_3 composite.

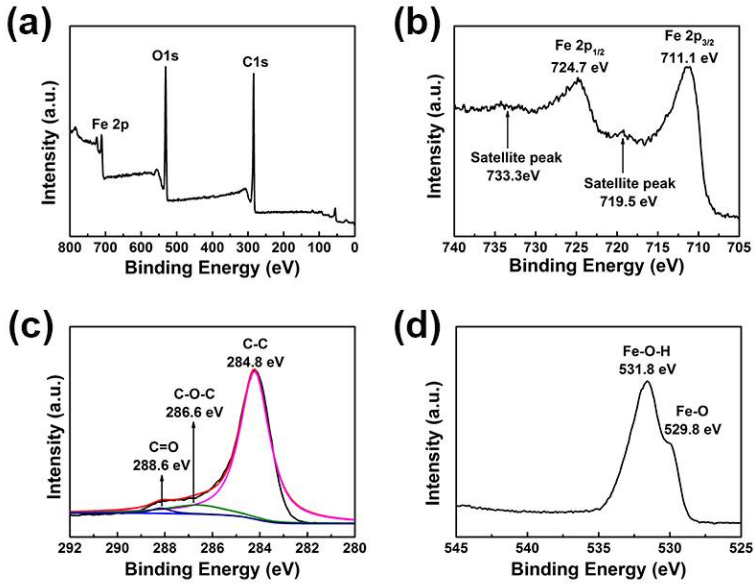

Figure 5. XPS full spectra (**a**), Fe 2p (**b**), C 1s (**c**), and (**d**) O 1s of the C@Fe_2O_3 composite.

The carbon content of the C@Fe_2O_3 composites was tested by thermogravimetric (TG) analysis. From the TG curve in Figure 6, the weight fraction of the carbon was recorded to be 46%. The specific surface area and pore size distribution of the C@Fe_2O_3 composite was obtained from nitrogen adsorption-desorption measurements. From Figure 7a, the isotherms indicate type IV hysteresis loops, with a marked hysteretic loop in a desorption branch between relative pressures P/P_0 of 0.8 and 0.95, corresponding to the mesoporous nature of the sample. In general, the type IV hysteresis loop typically occurs due to the aggregated nanoparticle structure. The BET surface area for the C@Fe_2O_3 composite was calculated at 85.56 m^2 g^{-1}. Figure 7b shows the Barrett-Joyner-Halenda (BJH) pore size adsorption plot for C@Fe_2O_3 sample, highlighting a bimodal-pore size centered at 3.7 nm and 49.9 nm. This further confirms the mesoporous morphology of C@Fe_2O_3 composites.

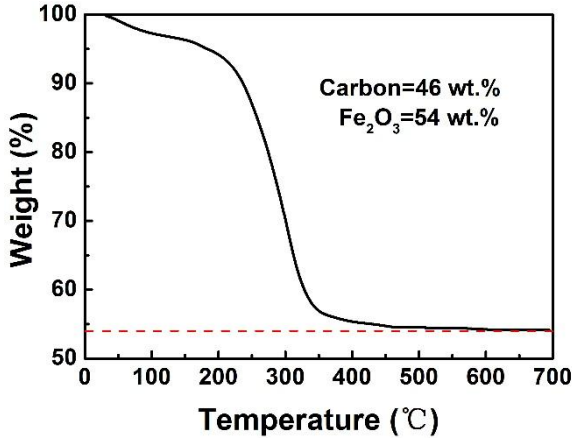

Figure 6. Thermogravimetric (TG) curve of the C@Fe_2O_3 composite.

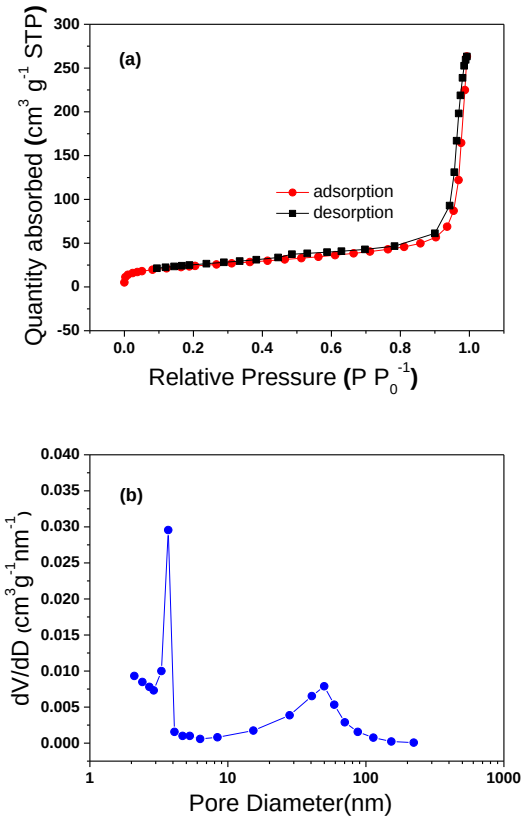

Figure 7. (**a**) Nitrogen adsorption/desorption isotherms and (**b**) the pore size distributions of C@Fe_2O_3 composites.

The electrochemical behavior of the C@Fe_2O_3 composite with Na-ion insertion-extraction was tested by cyclic voltammetry (CV) analysis as shown in Figure 8. In the cathodic scan, an irreversible peak is observed at around 0.75 V (vs. Na/Na^+), corresponding to the formation of a solid electrolyte interface (SEI) layer [16]. The pronounced reduction peak occurs near 0.08 V, which results in the reduction of the Fe_2O_3 [17]. In the anodic scan, two broad oxidation peaks are located at 0.46 V and 1.71 V, corresponding to the reversible oxidation of Fe^0 to Fe^{3+} [18]. The reversible electrochemical reaction can be described as [19]:

$$Fe_2O_3 + 6Na \leftrightarrow 2Fe + 3Na_2O \quad (1)$$

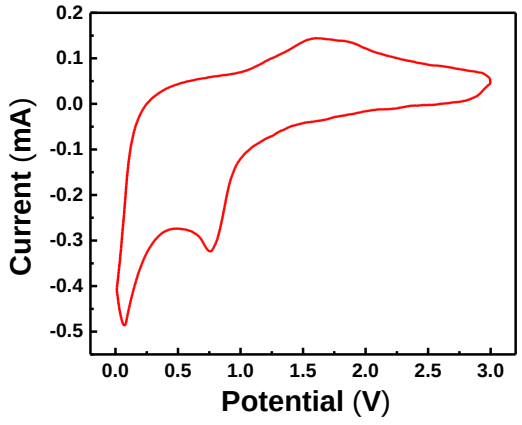

Figure 8. Cyclic voltammetry (CV) curve of the C@Fe_2O_3 composite at the initial cycle.

Figure 9 illustrates the charge–discharge profiles for the initial three cycles of the C@Fe_2O_3 composites at a current density of 50 mA g^{-1} and at a potential window between 0.01 and 3.0 V. As observed, the C@Fe_2O_3 composite delivers an initial discharge capacity of 709 mAh g^{-1} and a charge capacity of 415 mAh g^{-1}, which mainly originates in the first cycle, partially from the inevitable formation of the SEI film on the surface of the C@Fe_2O_3 electrode and the unique core-shell structure, which possesses a high specific surface area [20]. SEI films are generated from the decomposition of electrolyte, which produces a large amount of sodium ions and irreversibly intercalate into the crystal lattice [21]. In addition, no obvious voltage plateaus can be observed in Figure 9, which is accepted of Fe_2O_3 as is reported in the literature. Lastly, the capacity of the C@Fe_2O_3 composite quickly faded in the subsequent cycles because of the drastic volume change and the aggregation of Fe_2O_3 nanoparticles during charge-discharge processes [22].

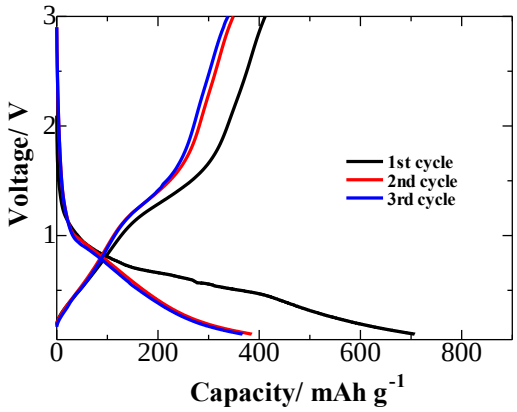

Figure 9. The charge-discharge profiles of the C@Fe_2O_3 composites at the initial three cycles at 50 mA g^{-1} between 0.01 and 3.0 V.

At a current density of 50 mA g^{-1} for 100 cycles, the cycling performances of C@Fe_2O_3 composite are shown in Figure 10. In the first cycle, the C@Fe_2O_3 composite manifests a high irreversible discharge capacity of 709 mAh g^{-1} and a relatively low initial coulombic efficiency of less than 60%. Subsequently, excellent cycle performance is maintained delivering a reversible capacity of 305 mAh g^{-1} for 100 cycles. Furthermore, along with a high reversible discharge capacity, excellent cyclability was demonstrated as well, and the capacity decay was only 0.22% in per cycle. Complimentarily, the C@Fe_2O_3 electrode delivers a coulombic efficiency of over 99%. In summary, these results imply an excellent reversibility of sodium insertion/deinsertion in the C@Fe_2O_3 composites.

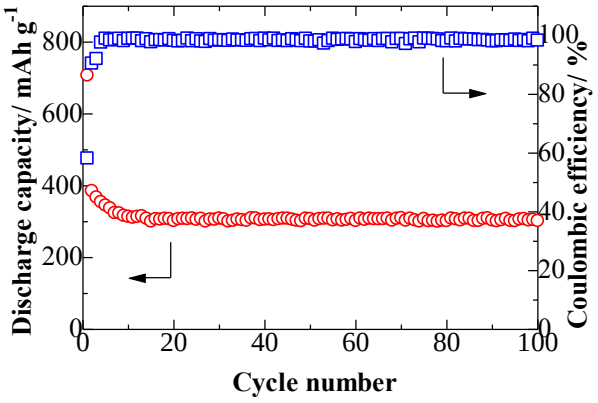

Figure 10. Cycling performance and coulombic efficiency of the C@Fe_2O_3 composites.

Figure 11 exhibits the rate capabilities of the C@Fe_2O_3 composite electrode at different current densities, spanning from 50 mA g^{-1} to 1000 mA g^{-1}. The C@Fe_2O_3 composite electrode demonstrates excellent rate performance and reversible capacities of 364, 291, 245, 206, and 150 mAh g^{-1} at current densities of 50, 100, 200, 500, and 1000 mA g^{-1}, respectively. Lastly, the C@Fe_2O_3 composite delivered a reversible capacity of 302 mAh g^{-1} when returning the current density back to the initial 50 mA g^{-1}. These results reveal that the stable core-shell structure of the carbon encapsulated Fe_2O_3 nanoparticles can effectively sustain the large volume change, alleviate the aggregation of Fe_2O_3 nanoparticles, and improve electronic transports during sodium insertion [16,23,24].

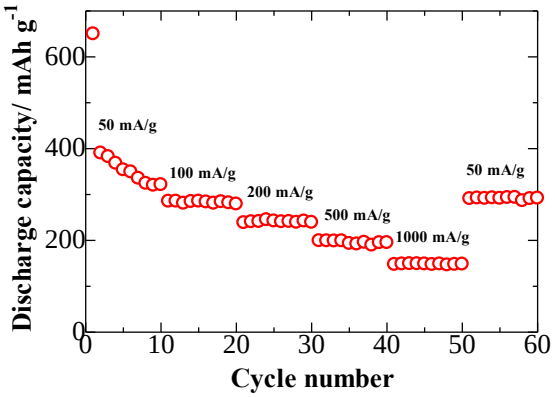

Figure 11. Rate performances of the C@Fe_2O_3 composites at various current densities.

Electrochemical impedance spectroscopy (EIS) measurements were measured to compare the Nyquist plots of C@Fe_2O_3 when fresh and after 100 cycles, as shown in Figure 12. The C@Fe_2O_3 composite, after 100 cycles, had much lower charge transfer resistance, corresponding to the smaller semicircle at high to middle frequency. As a result, the C@Fe_2O_3 composite exhibits a favorable electrochemical performance during cycling processes.

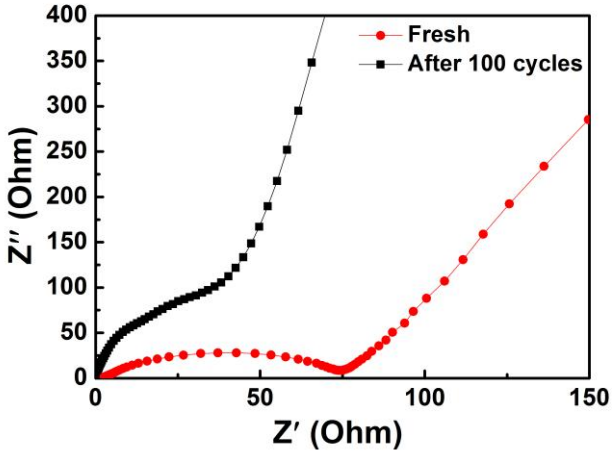

Figure 12. Impedance plots of the C@Fe_2O_3 composite when fresh and after 100 cycles.

The electrochemical performance of C@Fe_2O_3 composites obtained in this paper is better than those of previously reported results with Fe_2O_3 (Table 1) [12,25]. Compared with Fe_2O_3, the cycling performance of the C@Fe_2O_3 composites is much better, showing that the carbon contributes to the capacity of the C@Fe_2O_3 composites and the carbon is taking a positive effect.

Table 1. Comparison of the electrochemical performances of Fe_2O_3 and C@Fe_2O_3 composite for sodium-ion batteries.

Materials	Discharge Capacity (mAh g^{-1})	Cycle Number	Current Density (mAh g^{-1})	References
Fe_2O_3	16	10	50	[25]
α-Fe_2O_3	10	50	100	[12]
C@Fe_2O_3	305	100	50	This study

4. Conclusions

In summary, we reported a facile hydrothermal approach to fabricate a stable core-shell structure composed of carbon encapsulated Fe_2O_3 nanoparticles and investigated its application as anode materials for SIBs. A reversible capacity of 305 mAh g^{-1} can be obtained at 50 mA g^{-1} for up to 100 cycles for the C@Fe_2O_3 composites and it delivered a reversible capacity of 150 mAh g^{-1} at a current density of 1000 mA g^{-1}. When the current rate returned to 50 mA g^{-1}, the reversible capacity could recover up to 302 mAh g^{-1}, indicating high rate capabilities even at very high current densities. The electrochemical results demonstrated that the C@Fe_2O_3 composites feature excellent cycling performance and good rate capability due to the unique core-shell structure of the SIB anode.

Author Contributions: Formal Analysis, Y.Z.; Investigation, Y.Z.; Writing-Original Draft Preparation, T.T. and Y.Z.; Writing-Review & Editing, Z.B. and J.H.; Supervision, J.H.; Project Administration, T.T.; Funding Acquisition, Y.Z.

Funding: This research was funded by the China Postdoctoral Science Foundation (2018M630924); Program for the Outstanding Talents of Guangdong sailing plan, Human Resources and Social Security of Guangdong Province (201634007). ZB acknowledges support from a research project by the Ministry of Education and Science "Zinc based Rechargeable Aqueous Battery: A green, safe and economic battery for Space Applications" (AP05136016).

Conflicts of Interest: The authors declare no conflict of interest.

References

1. Firouzi, A.; Qiao, R.M.; Motallebi, S.; Valencia, C.W.; Israel, H.S.; Fujimoto, M.; Wray, L.A.; Chuang, Y.D.; Yang, W.L.; Wessells, C.D. Monovalent manganese based anodes and co-solvent electrolyte for stable low-cost high-rate sodium-ion batteries. *Nat. Commun.* **2018**, *9*, 861. [CrossRef] [PubMed]
2. Yuan, G.H.; Xiang, J.M.; Jin, H.F.; Jin, Y.Z.; Wu, L.Z.; Zhang, Y.G.; Mentbayeva, A.; Bakenov, Z. Flexible free-standing $Na_4Mn_9O_{18}$/reduced graphene oxide composite film as a cathode for sodium rechargeable hybrid aqueous battery. *Electrochim. Acta* **2018**, *259*, 647–654. [CrossRef]
3. Li, H.P.; Wei, Y.Q.; Zhang, Y.G.; Zhang, C.W.; Wang, G.K.; Zhao, Y.; Yin, F.X.; Bakenov, Z. In situ sol-gel synthesis of ultrafine ZnO nanocrystals anchored on graphene as anode material for lithium-ion batteries. *Ceram. Int.* **2016**, *42*, 12371–12377. [CrossRef]
4. Willis, T.J.; Porter, D.G.; Voneshen, D.J.; Uthayakumar, S.; Demmel, F.; Gutmann, M.J.; Roger, M.; Refson, K.; Goff, J.P. Diffusion mechanism in the sodium-ion battery material sodium cobaltate. *Sci. Rep.* **2018**, *8*, 3210. [CrossRef] [PubMed]
5. Chen, C.M.; Yang, Y.C.; Ding, S.S.; Wei, Z.X.; Tang, X.; Li, P.C.; Wang, T.H.; Cao, G.Z.; Zhang, M. S-doped carbon@TiO_2 to store Li^+/Na^+ with high capacity and long life-time. *Energy Storage Mater.* **2018**, *13*, 215–222. [CrossRef]
6. Teng, Y.Q.; Mo, M.S.; Li, Y.; Xue, J.L.; Zhao, H.L. Amorphous carbon-coated ZnO porous nanosheets: Facile fabrication and application in lithium- and sodium-ion batteries. *J. Alloys Compd.* **2018**, *744*, 712–720. [CrossRef]
7. Sultana, I.; Rahman, M.M.; Materi, S.; Ghanooni, A.V.; Glushenkov, A.M.; Chen, Y. K-ion and Na-ion storage performances of Co_3O_4-Fe_2O_3 nanoparticle-decorated super P carbon black prepared by a ball milling process. *Nanoscale* **2017**, *9*, 3646–3654. [CrossRef] [PubMed]
8. Fiore, M.; Longoni, G.; Santangelo, S.; Pantò, F.; Stelitano, S.; Frontera, P.; Antonucci, P.; Ruffo, R. Electrochemical characterization of highly abundant, low cost iron (III) oxide as anode material for sodium-ion rechargeable batteries. *Electrochim. Acta* **2018**, *269*, 367–377. [CrossRef]

9. Meng, S.; Zhao, D.L.; Wu, L.L.; Ding, Z.W.; Cheng, X.W.; Hu, T. Fe_2O_3/nitrogen-doped graphene nanosheet nanocomposites as anode materials for sodium-ion batteries with enhanced electrochemical performance. *J. Alloys Compd.* **2018**, *737*, 130–135. [CrossRef]
10. Liu, Y.C.; Wang, F.F.; Fan, L.Z. Self-standing Na-storage anode of Fe_2O_3 nanodots encapsulated in porous N-doped carbon nanofibers with ultra-high cyclic stability. *Nano Res.* **2018**, *1*, 1–12. [CrossRef]
11. Jiang, Y.; Hu, M.; Zhang, D.; Yuan, T.; Sun, W.; Xu, B.; Yan, M. Transition metal oxides for high performance sodium ion battery anodes. *Nano Energy* **2014**, *5*, 60–66. [CrossRef]
12. Zhang, Z.J.; Wang, Y.X.; Chou, S.L.; Li, H.J.; Liu, H.K.; Wang, J.Z. Rapid synthesis ofα-Fe_2O_3/rGO nanocomposites by microwave autoclave as superior anodes for sodium-ion batteries. *J. Power Sources* **2015**, *280*, 107–113. [CrossRef]
13. Gao, G.; Yu, L.; Wu, H.B.; Lou, X.W. Hierarchical tubular structures constructed by carbon-coated α-Fe_2O_3 nanorods for highly reversible lithium storage. *Small* **2014**, *10*, 1741–1745. [CrossRef] [PubMed]
14. Li, H.P.; Li, Y.; Zhang, Y.G.; Zhang, C.W. Facile synthesis of carbon-coated Fe_3O_4 core-shell nanoparticles as anode materials for lithium-ion batteries. *J. Nanopart. Res.* **2015**, *17*, 370. [CrossRef]
15. Zhang, Y.G.; Li, Y.; Li, H.P.; Zhao, Y.; Yin, F.X.; Bakenov, Z. Electrochemical performance of carbon-encapsulated Fe_3O_4 nanoparticles in lithium-ion batteries: Morphology and particle size effects. *Electrochim. Acta* **2016**, *216*, 475–483. [CrossRef]
16. Jian, Z.L.; Zhao, B.; Liu, P.; Li, F.J.; Zheng, M.B.; Chen, M.W.; Shi, Y.; Zhou, H.S. Fe_2O_3 nanocrystals anchored onto graphene nanosheets as the anode material for low-cost sodium-ion batteries. *Chem. Commun.* **2014**, *50*, 1215–1217. [CrossRef] [PubMed]
17. Zhang, N.; Han, X.; Liu, Y.; Hu, X.; Zhao, Q.; Chen, J. 3D porous γ-Fe_2O_3@C nanocomposite as high-performance anode material of Na-ion batteries. *Adv. Energy Mater.* **2015**, *5*, 1401123–1401130. [CrossRef]
18. Wu, Z.G.; Zhong, Y.J.; Liu, J.; Wu, J.H.; Guo, X.D.; Zhong, B.H.; Zhang, Z.Y. Subunits controlled synthesis of α-Fe_2O_3 multi-shelled core-shell microspheres and their effects on lithium/sodium ion battery performances. *J. Mater. Chem. A* **2015**, *3*, 10092–10099. [CrossRef]
19. Philippe, B.; Valvo, M.; Lindgren, F.; Rensmo, H.; Edstrom, K. Investigation of the Electrode/Electrolyte Interface of Fe_2O_3 Composite Electrodes: Li vs Na Batteries. *Chem. Mater.* **2014**, *26*, 5028–5041. [CrossRef]
20. Wang, S.B.; Wang, W.; Zhan, P.; Jiao, S.Q. Hollow alpha-Fe_2O_3 nanospheres synthesized using a carbon template as novel anode materials for Na-ion batteries. *ChemElectroChem* **2014**, *1*, 1636–1639. [CrossRef]
21. Valvo, M.; Lindgren, F.; Lafont, U. Towards more sustainable negative electrodes in Na-ion batteries via nanostructured iron oxide. *J. Power Sources* **2014**, *245*, 967–978. [CrossRef]
22. Xu, X.; Cao, R.; Jeong, S.; Cho, J. Spindle-like mesoporous α-Fe_2O_3 anode material prepared from MOF template for high-rate lithium batteries. *Nano Lett.* **2012**, *12*, 4988–4991. [CrossRef] [PubMed]
23. Su, D.W.; Ahn, H.J.; Wang, G.X. SnO_2@graphene nanocomposites as anode materials for Na-ion batteries with superior electrochemical performance. *Chem. Commun.* **2013**, *49*, 3131–3133. [CrossRef] [PubMed]
24. Wang, W.; Hu, L.W.; Ge, J.B.; Hu, Z.Q.; Sun, H.B.; Sun, H.; Zhang, H.Q.; Zhu, H.M.; Jiao, S.Q. In situ self-assembled $FeWO_4$/graphene mesoporous composites for Li-ion and Na-ion batteries. *Chem. Mater.* **2014**, *26*, 3721–3730. [CrossRef]
25. Liu, X.J.; Chen, T.Q.; Chu, H.P.; Niu, L.Y.; Sun, Z.; Pan, L.K.; Sun, C.Q. Fe_2O_3-reduced graphene oxide composites synthesized via microwave-assisted method for sodium ion batteries. *Electrochim. Acta* **2015**, *166*, 12–16. [CrossRef]